

Chapter 2

Structures and Optical Properties of Pt and Pd Compounds with Charge-Density-Waves

Hiroshi Okamoto and Hiroyuki Matsuzaki

2.1 Introduction

Dynamics of excitons and photocarriers in one-dimensional (1D) semiconductors have been attracting much attention from both theoretical and experimental point of views. In 1D electronic systems, it is known that the excitonic effect is remarkably enhanced due to the singularity of the 1D Coulomb potential. The effect of the electron–lattice (e–l) interaction is also important in 1D electronic systems as exemplified by the Peierls transition. It was theoretically expected that a free exciton (FE) is easily relaxed to a self-trapped exciton (STE) via lattice relaxations, since there is no barrier between an FE and an STE in 1D systems [1]. In 1D half-filled electronic systems, it is known that the e–l interaction sometimes plays a significant role on their electronic structures and charge dynamics. A typical example of such an e–l coupled system is *trans*-polyacetylene (*trans*-(CH)_x), in which the dimerization or equivalently the bond alternation occurs via the Peierls mechanism [2]. In *trans*-(CH)_x, it is known that charge and/or spin carriers are stabilized as solitons [3, 4] or polarons under the influence of the e–l interaction, which exhibit characteristic midgap absorptions. Thus, clarifying the nature of solitons and polarons as well as of excitons is essential for understanding optical and transport properties of the 1D e–l coupled systems. In general, conjugated polymers including (CH)_x cannot be obtained as single crystals and

H. Okamoto (✉)

Department of Advanced Materials Science, Faculty of Frontier Sciences, University of Tokyo,
5-1-5 Kashiwanoha, Kashiwa, Chiba 277-8561, Japan
e-mail: okamotoh@k.u-tokyo.ac.jp

H. Matsuzaki

Department of Advanced Materials Science, Faculty of Frontier Sciences, University of Tokyo,
5-1-5 Kashiwanoha, Kashiwa, Chiba 277-8561, Japan

Research Institute of Instrumentation Frontier, National Institute of Advanced Industrial Science and Technology (AIST), Tsukuba Central 5, 1-1-1 Higashi, Tsukuba, Ibaraki 305-8565, Japan

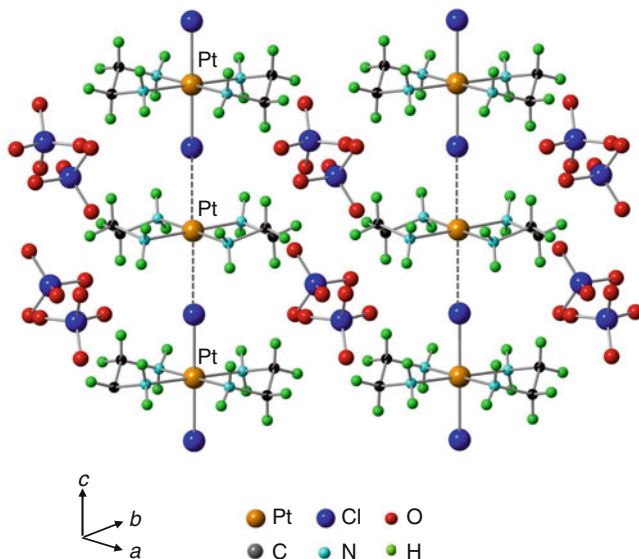


Fig. 2.1 Structure of $[\text{Pt}(\text{en})_2][\text{Pt}(\text{en})_2\text{Cl}_2](\text{ClO}_4)_4$

their electronic states are not so controllable. Therefore, it is difficult to perform systematic studies of excitons, solitons, and polarons in those systems.

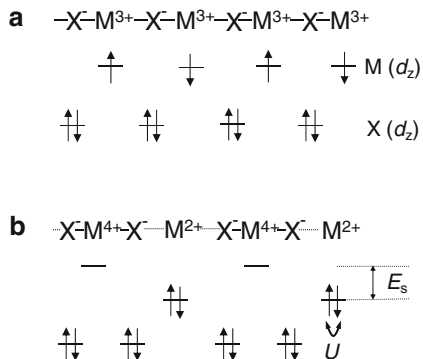
Subsequently, halogen(X)-bridged transition metal(M) compounds (or equivalently MX-chain compounds) have provided a unique opportunity to study the nature of excitons, solitons, and polarons [5]. A great advantage of this category of materials is that their electronic structures can be widely controlled and a variety of materials can be obtained as single crystals. As a result, a number of studies concerning excitons, solitons, and polarons have been reported so far in MX-chain compounds [6–52].

MX-chain compounds are represented as $[\text{MA}_2][\text{MA}_2\text{X}_2]\text{Y}_4$ (or simply $\{\text{MA}_2\text{X}\}\text{Y}_2$), where A and Y are the ligand and the counter anion, respectively. The crystal structure of $[\text{Pt}(\text{en})_2][\text{Pt}(\text{en})_2\text{Cl}_2](\text{ClO}_4)_4$ (en = ethylenediamine) is shown in Fig. 2.1 as a typical example of MX-chain compounds. As shown in the figure, the $[\text{MA}_2]$ moieties are bridged by the halogen ions (X) and the hydrogen (H)-bonds between the amino groups of the ligands (A) and the counter anions (Y) support the MX chains. In the compounds with $\text{M} = \text{Pt}$ and Pd , $\text{M}(\text{II})$ and $\text{M}(\text{IV})$ mixed-valence state, or equivalently, the commensurate charge-density-wave (CDW) state is stabilized due to the strong e–I interaction, while in the compounds with $\text{M} = \text{Ni}$, $\text{Ni}(\text{III})$ mono-valence state, or equivalently, the Mott–Hubbard (MH) state appears [53–55]. As detailed in Chap. 4, a $\text{Pd}(\text{III})$ MH compound has also been recently synthesized.

In the Pt and Pd compounds, amplitudes of CDW can be controlled by the replacements of metals ($\text{M} = \text{Pt}$ and Pd), bridging halogens ($\text{X} = \text{Cl}$, Br , and I), ligand molecules ($\text{A} = \text{ethylenediamine (en)}$, ethylamine, diaminocyclohexane (chxn), etc.) and counter anions ($\text{Y} = \text{ClO}_4$, BF_4 , Cl , Br , I , etc.) surrounding the MX chains [28, 32]. In addition, the nondegenerate CDW states can be obtained in

Fig. 2.2 Schematic electronic structure of the MX chain.

(a) The mono-valence (Mott–Hubbard) state and
(b) the mixed-valence (CDW) state



the heterometal compounds in which Pt and Pd ions arrange alternatively [26, 52]. Such a controllability of CDW in MX-chain compounds allows us to make an advanced study of dynamics of excitons, solitons, and polarons.

In this chapter, firstly, we review how the CDW ground state can be controlled by the choice of constituent elements (M, X, A, and Y). Secondly, we summarize the fundamental optical properties of the CDW compounds, focusing on the optical absorption and photoluminescence (PL) properties, which are dominated by the transition to the lowest charge-transfer (CT) exciton and the emission from the self-trapped exciton (STE), respectively. After that, we detail nature of solitons and polarons investigated by the photoinduced absorption (PA) spectroscopy. From the comparison of PL properties from STEs and PA spectra due to solitons and polarons, we discuss the relaxation dynamics of photoexcited states in MX-chain compounds in the CDW phase.

2.2 Control of CDW Ground States [5, 32]

In MX-chain compounds, 1D electronic state of an MX chain consists of d_{z^2} orbitals of M and p_z orbitals of X. The ground state is the mono-valence M(III) state or the mixed-valence M(II) and M(IV) state (or equivalently the commensurate CDW state) as shown in Figs. 2.2a, b, respectively. In Pt and Pd compounds, the mono-valence state is usually unstable due to the site-diagonal-type e–l interaction overcoming the on-site Coulomb repulsion energy U on the metal site [8, 9]. In Ni compounds, the mono-valence state is stabilized due to the large U on the Ni sites, so that their electronic structure is considered to be the Mott–Hubbard (MH) insulator state [53, 54]. More precisely, the Ni compounds belong to the CT insulators in which the transition from the halogen p valence band to the Ni 3d upper Hubbard band corresponds to the optical gap [55]. CDW states are never stabilized in the Ni compounds. In this section, we show that CDW states (amplitudes of CDW, degeneracy of CDW, and optical gap energies) in Pt and Pd compounds can be widely controlled by the choice of constituent elements in MX-chain compounds.

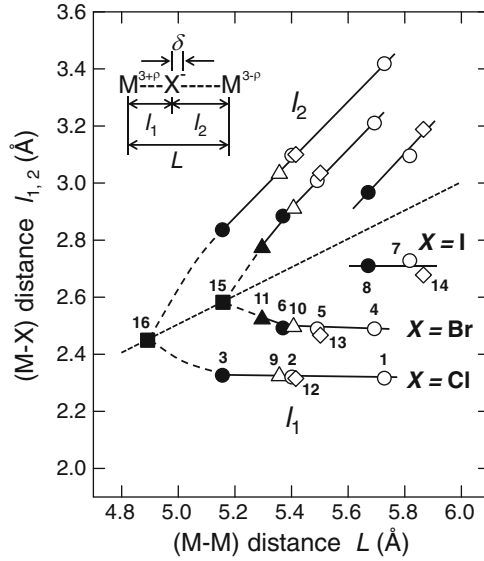


Fig. 2.3 Correlation between the M-M distance (L) and the M-X distance (l_1 and l_2). The material for each number is listed in Table 2.1. Data of the homometal compounds are represented by circles for $M = \text{Pt}$, triangles for $M = \text{Pd}$, and squares for $M = \text{Ni}$. Data of the heterometal compounds with $M = \text{Pt}$ and Pd are represented by diamonds. Open and filled marks indicate the compounds with $Y = \text{ClO}_4$ and $Y = \text{halogen}$, respectively. (Reprinted figure with permission from [5])

2.2.1 Control of CDW Amplitudes

By replacing metals ($M = \text{Pt}$ or Pd) and bridging halogens ($X = \text{Cl}$, Br , or I), the Coulomb repulsion energy (U) on the metal site and the transfer energy (t) between the nearest-neighbor two metal sites can be considerably changed. It is because the expanses of d_{z^2} orbitals of M and p_z orbitals of X are different among the respective metal ions (M) and bridging halogen ions (X) [13, 32]. As a result, we can obtain a variety of compounds having different bridging halogen displacements δ from the midpoint between the neighboring two M ions (see the inset of Fig. 2.3). The systematic structural studies revealed that δ is closely correlated to the metal to metal (M-M) distance L , which is strongly dependent on the choice of the ligand (A) and the counter anion (Y) and also on the strength of the H-bond between A and Y [32].

In Table 2.1, the M-M distance L , the metal to halogen (M-X) distance l_1 and l_2 ($l_1 < l_2$), the halogen displacement δ ($l_2 - l_1 = 2\delta$), and the distortion parameter d ($d = 2\delta/L$) are listed for various MX-chain compounds. In Fig. 2.3, the values of l_1 and l_2 are plotted as a function of L . The dotted line indicates $l_1 = l_2 = L/2$, which is a hypothetical line for no bridging halogen displacements ($\delta = 0$). The Ni compounds having the MH states are located on this line. The deviation of l_1 and l_2 from the dotted line corresponds to a magnitude of δ . The most significant feature in Fig. 2.3 is that the data points fall on almost the same lines according to the choice of bridging halogen (X) ions (Cl^- , Br^- or I^-), while M , A , and Y are replaced. It indicates the strong correlation between δ and L .

Table 2.1 The M–M distance L , the M–X distance l_1 and l_2 ($l_1 < l_2$), the bridging halogen displacement δ ($= (l_2 - l_1)/2$), the distortion parameter d ($= 2\delta/L$), the CT-exciton energy E_{CT} , and the photoluminescence energy E_{lm} for various MX-chain compounds

		L (Å)	l_1 (Å)	l_2 (Å)	δ (Å)	d	E_{CT} (eV)	E_{lm} (eV)
1.	[Pt(chxn) ₂][Pt(chxn) ₂ Cl ₂](ClO ₄) ₄	5.730	2.314	3.416	0.511	0.190	3.20	1.49
2.	[Pt(en) ₂][Pt(en) ₂ Cl ₂](ClO ₄) ₄	5.403	2.318	3.095	0.3885	0.144	2.73	1.17
3.	[Pt(chxn) ₂][Pt(chxn) ₂ Cl ₂]Cl ₄	5.158	2.324	2.834	0.255	0.099	1.99	0.90
4.	[Pt(en) ₂][Pt(en) ₂ Br ₂](ClO ₄) ₄ -I	5.493	2.487	3.006	0.2595	0.094	1.98	0.78
5.	[Pt(en) ₂][Pt(en) ₂ Br ₂](ClO ₄) ₄ -II	5.695	2.487	3.208	0.3605	0.1266	2.40	1.11
6.	[Pt(chxn) ₂][Pt(chxn) ₂ Br ₂]Br ₄	5.372	2.490	2.882	0.196	0.073	1.40	0.68
7.	[Pt(en) ₂][Pt(en) ₂ I ₂](ClO ₄) ₄	5.820	2.726	3.093	0.1835	0.063	1.38	0.60
8.	[Pt(chxn) ₂][Pt(chxn) ₂ I ₂]I ₄	5.673	2.708	2.965	0.2564	0.0453	0.94	–
9.	[Pd(en) ₂][Pt(en) ₂ Cl ₂](ClO ₄) ₄	5.357	2.324	3.003	0.3545	0.130	2.05	0.86
10.	[Pd(en) ₂][Pd(en) ₂ Br ₂](ClO ₄) ₄	5.407	2.911	2.496	0.2075	0.075	1.13	0.40
11.	[Pd(chxn) ₂][Pd(chxn) ₂ Br ₂]Br ₄	5.296	2.523	2.773	0.125	0.047	0.75	–
12.	[Pd(en) ₂][Pt(en) ₂ Cl ₂](ClO ₄) ₄	5.415	2.315	3.100	0.3925	0.145	3.22	1.65
13.	[Pd(en) ₂][Pt(en) ₂ Br ₂](ClO ₄) ₄	5.502	2.467	3.035	0.284	0.103	2.59	1.54
14.	[Pd(en) ₂][Pt(en) ₂ I ₂](ClO ₄) ₄	5.866	2.678	3.188	0.255	0.087	2.28	1.12
15.	[Ni(chxn) ₂ Cl ₂]Cl ₂	4.894	2.447		0	0	1.83	–
16.	[Ni(chxn) ₂ Br ₂]Br ₂	5.160	2.580		0	0	1.28	–

Parameter values are taken from [5] and references therein

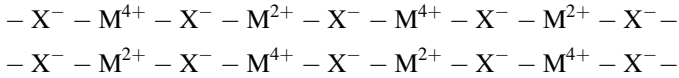
Typical MX-chain compounds have ClO₄[−] for the counteranion (Y). The data of those compounds are shown by open marks in Fig. 2.3. The data of the compounds with halogen ions for Y are plotted by solid marks in the same figure. By changing the counteranion from ClO₄[−] to halogen ions, the H-bonds between the amino groups of the ligands and the counteranions are strengthened. As a result, the M–M distance L is considerably decreased. Such a feature was ascertained by the infrared (IR) and X-ray measurements [28, 32, 56]. As shown in Fig. 2.3, the lengths L in the compounds with Y = halogen (solid marks) are relatively smaller than those of the compounds with Y = ClO₄ (open marks).

The position of the bridging halogen (X) ion between the neighboring two M ions, or the M–X distance l_1 and l_2 , depends strongly on the choice of X. As seen in Fig. 2.3, the shorter M–X distance l_1 is almost constant in Pt or Pd compounds having the same X ions, even when L is considerably changed. The constant values of l_1 (~ 2.33 Å for X = Cl and ~ 2.50 Å for X = Br, $2.68 \sim 2.73$ Å for X = I) are close to the sum of the ionic radii of the bridging halogen ions (Cl[−]: 1.81 Å, Br[−]: 1.96 Å and I[−]: 2.16 Å [57, 58]) and the metal (Pd⁴⁺: 0.62 Å and Pt⁴⁺: 0.63 Å [59]). Starting from the M³⁺–X[−] regular chain structure, the deviation of l_1 from the dotted line ($L/2$) corresponds to the amplitude of the halogen displacements δ . Therefore, the decrease of L induces the decrease of the longer M–X distance l_2 , and then induces the decrease of δ . Thus, we can consider that the decrease of L suppresses effectively the e–I interaction. At the same time, the decrease of L leads to the increase of transfer energy (t) between the neighboring M ions, making the electronic state more delocalized and also decreasing δ , that is, the CDW

amplitude. The increase of l_1 (the deviation from the constant value of l_1) in [Pd(chxn)₂Br]Br₂ (No. 11 in Fig. 2.3) located near the CDW-MH phase boundary is attributable to such an increase of t [28].

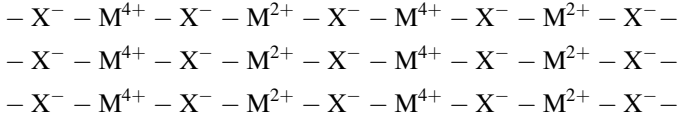
2.2.2 Control of CDW Degeneracy

MX compounds have the doubly degenerate CDW ground states, which are expressed as follows.



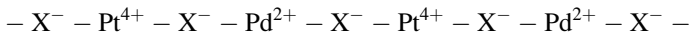
This degeneracy of CDW can also be modified by the choice of constituent elements.

In the CDW compounds with halogen for the counteranion (Y), a direction of each halogen displacement is two-dimensionally ordered in the bc plane [28, 32], as shown below.



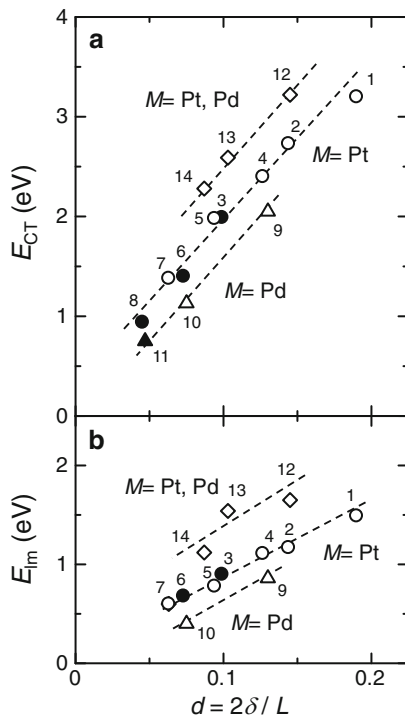
This is not due to the overlapping of the electronic states between the neighboring MX chains but due to the interchain coupling through the tight network of the H-bonds between the aminogroups of the ligands (A) and the counter halogen ions (Y). Thus, although the electronic states are still one-dimensional, a 2D ordering of CDW is formed.

Degeneracy of CDW states can be excluded more clearly by the metal alternation method. By substituting a half of Pt ions with Pd ions in $M = \text{Pt}$ compounds, we can obtain the heterometal compounds in which Pt and Pd ions are arranged alternatively [26]. In those compounds, the 1D electronic state consists of the 4d orbitals of Pd and the 5d orbitals of Pt. As the energy level of the former is lower than the latter, the CDW state is formed by Pd²⁺ ions and Pt⁴⁺ ions, as shown below.



In this type of the heterometal compounds, CDW states are nondegenerate. The lattice parameters, L , l_1 and l_2 for the heterometal compounds were also plotted in Fig. 2.3 by diamonds. The deviation of the data points from those of the homometal

Fig. 2.4 Energies of (a) CT-exciton absorption peaks (E_{CT}) and (b) STE luminescence peaks (E_{lm}) as a function of the distortion parameter d . The material for each number is listed in Table 2.1. Data of the Pt compounds are represented by circles. Data of the heterometal compounds with $M = \text{Pt}$ and Pd are represented by diamonds. Open and filled marks indicate the compounds with $Y = \text{ClO}_4$ and $Y = \text{halogen}$, respectively. (Reprinted figure with permission adapted from [5])



Pt or Pd compounds is very small. It is because L is determined mainly by the choice of the ligand (A), the counter anion (Y), and the bridging halogen ions (X), and l_1 is almost equal to the sum of the ion radii of Pt^{4+} and X^- ions as mentioned above.

It provides serious modifications to relaxation processes of photoexcited states in the MX chains whether CDW is degenerate or nondegenerate; in degenerate CDW states, solitons are the low-energy excitations and play dominant roles on the relaxation processes but in nondegenerate CDW states, formations of solitons are suppressed. Relaxation processes of photoexcited states associated with solitons are discussed in Sect. 2.3.2.

2.2.3 Control of Optical Gap Energies

In the MX-chain compounds, the lowest optical transition corresponding to the optical gap is the charge-transfer (CT) exciton transition expressed as $(\text{M}^{2+}, \text{M}^{4+} \rightarrow \text{M}^{3+}, \text{M}^{3+})$ [13, 32]. In Table 2.1, the energies of those transitions (E_{CT}) are listed for the various compounds. In Fig. 2.4a, E_{CT} is plotted for Pt and Pd compounds, and the heterometal ($M = \text{Pt}$ and Pd) compounds as a function of the distortion parameter

d ($d = 2\delta/L$). E_{CT} is mainly determined by the energy difference E_s between the M^{2+} site and the M^{4+} site shown in Fig. 2.2b. In the compounds having the same metal ions, we can see the linear relation between E_{CT} and d , which indicates that E_s is proportional to the halogen displacement δ .

E_{CT} in Pd compounds is smaller than that in Pt compounds. This trend is related to the magnitude of the on-site Coulomb repulsion energy U . In the localized limit shown in Fig. 2.2a, E_{CT} is proportional to $(E_s - U)$. Since U is larger in the Pd compounds than in the Pt compounds, E_{CT} in the former is lower than in the latter. In the heterometal compounds with $M = \text{Pt}$ and Pd , E_{CT} is relatively larger than that in the homometal compounds with $M = \text{Pt}$. This is attributable to the energy difference between the 4d orbitals of Pd^{2+} and 5d orbitals of Pt^{2+} , since the energy level of the former is lower than the latter.

From the results of Fig. 2.3 showing the X, A, and Y dependence of δ and the results of Fig. 2.4a showing the M dependence of E_{CT} , we can widely control the magnitudes of E_{CT} by the choice of M, X, A, and Y.

2.3 Nature and Dynamics of Excitons, Solitons, and Polarons

Photogeneration and relaxation of excitons, solitons, and polarons in MX-chain compounds are strongly dependent on the optical gap energies E_{CT} and the bridging halogen displacements δ . In Sect. 2.3.1 we review the PL properties from STEs depending on E_{CT} and δ . In Sect. 2.3.2, we show how photogenerated solitons and polarons can be detected. In Sect. 2.3.3, we discuss the conversion process of an exciton to a spin-soliton pair. In Sect. 2.3.4, we summarize the overall relaxation dynamics of photoexcited states associated with excitons, solitons, and polarons in MX-chain compounds.

2.3.1 Self-Trapped Excitons

In MX-chain compounds, PL from STEs is observed in common. In Fig. 2.5, the PL spectrum of $[\text{Pt}(\text{en})_2][\text{Pt}(\text{en})_2\text{Cl}_2](\text{ClO}_4)_4$ at 2 K was shown as a typical example [11]. The PL peak is located at 1.2 eV, showing a large Stokes shift of about 1.5 eV. Such a large Stokes shift comes from the large lattice relaxation energy of the STE, which originates from the dissolution of the bridging halogen displacements as illustrated in Fig. 2.6a. Adiabatic potential energies of an exciton (FE and STE) as a function of the deformation coordinate Q (the displacements of the bridging X ions from their equilibrium positions in the CDW ground state) were also schematically shown in Fig. 2.6b. At the higher energy side of the PL, a series of 17 sharp structures due to Raman scattering bands are observed (Fig. 2.5), which correspond to the symmetric-stretching mode of bridging Cl ions. The appearance of the higher order Raman bands also indicates the strong e-l interaction of this compound.

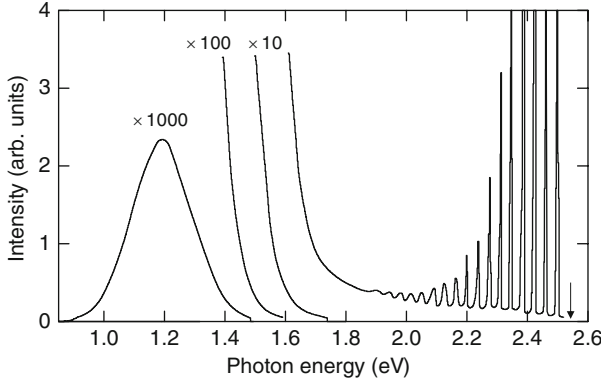


Fig. 2.5 Photoluminescence and Raman bands in $[\text{Pt}(\text{en})_2][\text{Pt}(\text{en})_2\text{Cl}_2](\text{ClO}_4)_4$ at 2 K. The excitation photon energy (2.54 eV) is indicated by the arrow. (Reprinted figure with permission from [11])

Dynamics of STE was studied by time-resolved PL measurements [60–62]. Figure 2.7 shows the time evolutions of PL at several probe energies in $[\text{Pt}(\text{en})_2][\text{Pt}(\text{en})_2\text{Br}_2](\text{ClO}_4)_4\text{-I}$. The oscillatory structures were observed and attributed to the wave-packet motion in the potential curve as shown by the arrow in Fig. 2.6b. A similar oscillation was also detected in $[\text{Pt}(\text{en})_2][\text{Pt}(\text{en})_2\text{Br}_2](\text{PF}_6)_4$ by using transient absorption technique [63].

Next, we discuss how the PL properties depend on materials. The energies of PL (E_{lm}) for various MX compounds were also listed in Table 2.1 and plotted against the distortion parameter d in Fig. 2.4b [5]. E_{lm} is 40–50 % of E_{CT} for the Pt or Pd compounds and 50–60 % for the heterometal compounds with $\text{M} = \text{Pt}$ and Pd , showing large Stokes shifts in common. On the other hand, the efficiency of PL is considerably changed by the decrease in gap energy E_{CT} . In Fig. 2.8, the relative intensities of PL for the 2.4-eV excitation measured at 2 K are plotted for various MX compounds [5]. The intensity of PL decreases by more than four orders of magnitude when E_{CT} decreases from 2.7 to 1.4 eV. This result suggests that with decrease of E_{CT} , that is, the halogen distortion δ , the STE becomes unstable. Another feature in Fig. 2.8 is that the PL intensity in the compounds with nondegenerate CDW [the heterometal compounds (diamonds) and the Pt compounds with the 2D ordered CDW (solid circles)] is relatively larger than those of the Pt compounds with 1D CDW. This is related to the fact that nonradiative recombination of photoexcited states via soliton formations is suppressed in nondegenerate CDW compounds. This point is discussed in the following subsections.

2.3.2 Photogeneration of Solitons and Polarons

In this section, we review the studies of solitons and polarons in the MX-chain compounds. The most effective method to detect solitons and polarons is a

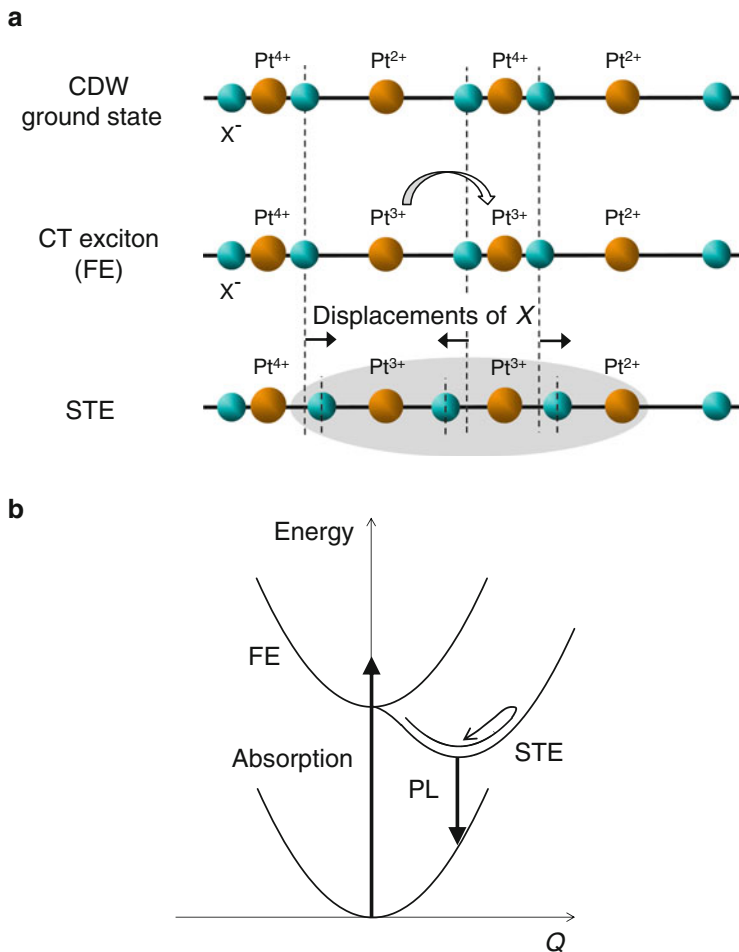


Fig. 2.6 (a) Schematic of the CDW ground state, the CT exciton (FE), and the STE. (b) Schematic of the adiabatic potential curves of the CT exciton (FE) and the STE as a function of the deformation coordinate (see the text)

photoinduced absorption (PA) spectroscopy, which had been indeed used for the studies of solitons, polarons, and bipolarons in conjugated polymers [2], and a number of important information were obtained. Photoinduced electron spin resonance (PESR) could also detect sensitively photoexcited species with spins. Those measurements were performed on the MX-chain compounds to clarify nature of photogenerated species.

At the beginning of those studies, the Pt–Cl chain compound, $[\text{Pt}(\text{en})_2][\text{Pt}(\text{en})_2\text{Cl}_2](\text{ClO}_4)_4$, had been extensively studied. In this compound, however, photoinduced gap states were very stable and not mobile so that they never decayed at low temperatures once they were photogenerated. Therefore, it was difficult to

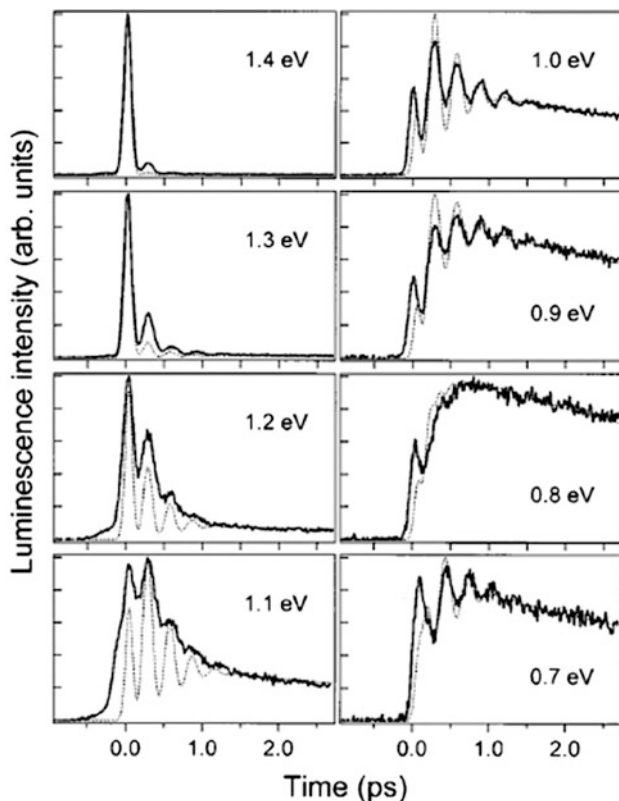


Fig. 2.7 Time evolutions of the luminescence intensity in $[\text{Pt}(\text{en})_2][\text{Pt}(\text{en})_2\text{Br}_2](\text{ClO}_4)_4\text{-I}$. The experimental results are shown by *solid lines*. *Dotted lines* show the simulations (see [61]). (Reprinted figure with permission from [61]. Copyright (1999) by the American Physical Society)

investigate nature and dynamical aspects of the gap states in that compound. To solve this problem, Pt–Br and Pt–I chain compounds were subsequently studied, in which photoinduced gap states are mobile and their dynamical aspects could be clarified. Here, we introduce the comparative studies of the homometal compound, $[\text{Pt}(\text{en})_2][\text{Pt}(\text{en})_2\text{Br}_2](\text{ClO}_4)_4\text{-II}$, and the heterometal compound, $[\text{Pd}(\text{en})_2][\text{Pt}(\text{en})_2\text{Br}_2](\text{ClO}_4)_4$, using PA and PESR measurements [52]. As mentioned in Sect. 2.2.2, the CDW ground states are degenerate in the former and nondegenerate in the latter, so that solitons are stabilized only in the former. Such a difference in the two compounds enables us to obtain a clear evidence for the photogeneration of solitons. In $[\text{Pt}(\text{en})_2][\text{Pt}(\text{en})_2\text{Br}_2](\text{ClO}_4)_4$, two monoclinic polymorphisms with the space group $P2_1/m$ and $C2/m$ were obtained [10, 11] and labeled as I and II, respectively, as already used. Hereafter, $[\text{Pt}(\text{en})_2][\text{Pt}(\text{en})_2\text{Br}_2](\text{ClO}_4)_4\text{-II}$ and $[\text{Pd}(\text{en})_2][\text{Pt}(\text{en})_2\text{Br}_2](\text{ClO}_4)_4$ are abbreviated as Pt–Br–Pt-II and Pd–Br–Pt, respectively.

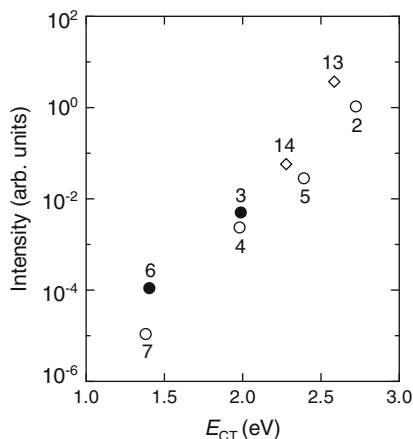


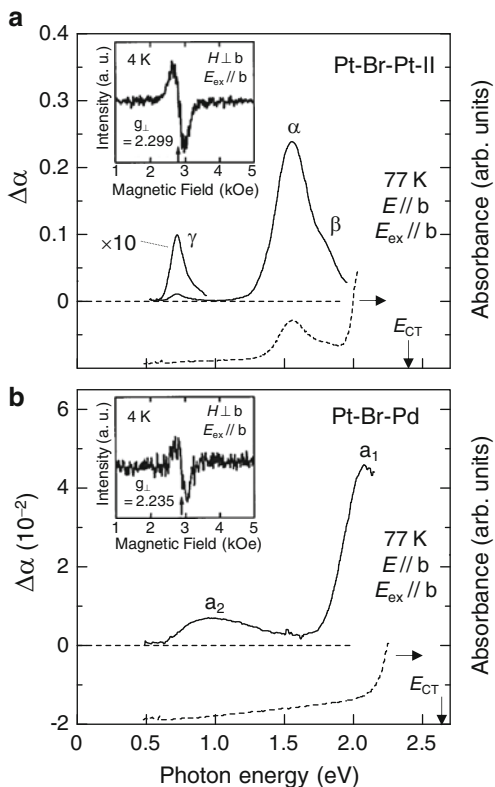
Fig. 2.8 Normalized integrated intensities of the luminescence as a function of E_{CT} in the MX chain compounds. The material for each number is listed in Table 2.1. Luminescence is measured at 2 K with the excitation photon energy of 2.4 eV. Data of the Pt compounds are represented by circles. Data of the heterometal compounds with M = Pt and Pd are represented by diamonds. Open and filled marks indicate the compounds with Y = ClO₄ and Y = halogen, respectively. (Reprinted figure with permission from [5])

Figure 2.9a shows the PA spectrum $\Delta\alpha$ (photoinduced change of $\alpha = kl$) of [Pt(en)₂][Pt(en)₂Br₂](ClO₄)₄-II single crystal with the excitation of 3.2 eV at 77 K. Here, k and l are the absorption coefficient and the sample thickness, respectively. Polarization of both the irradiation light (E_{ex}) and the transmission light (E) is parallel to the chain axis b . In Fig. 2.9a, the polarized absorption spectrum for $E//b$ was also shown by the broken line. The arrow indicates the optical gap energy E_{CT} . A midgap absorption band labeled as α at 1.55 eV and a weak shoulder structure labeled as β at 1.79 eV were observed in as-grown samples. These absorption bands were enhanced by light irradiations. In addition, a weak PA band labeled as γ was observed at 0.7 eV. To discriminate the observed PA bands, time characteristics of three structures were investigated. The results showed that bands α and β exhibited the same decay characteristics, while band γ decays in a different manner compared with α and β . These results suggest that optically excited states include two different photoproducts associated with α , β , and with the lower energy band γ .

The absorption and PA spectra in the heterometal compound, Pt-Br-Pd, were shown in Fig. 2.9b. They were considerably different from the spectra in Pt-Br-Pt-II. In the absorption spectrum below the optical gap energy E_{CT} , there were no prominent structures. By the 3.2 eV excitation, two PA bands appeared, which were labeled as a_1 and a_2 . a_1 and a_2 were found to show the same decay characteristics, suggesting that they are related to the same excited species.

To deduce the generation process of the photoproducts, excitation profiles of PA bands (α and γ in Pt-Br-Pt-II, and a_1 in Pt-Br-Pd) were measured. The results are shown in Fig. 2.10 by circles for band α , triangles for band γ in Pt-Br-Pt-II, and the

Fig. 2.9 PA spectra with the excitation of 3.2 eV and polarized absorption spectrum (*broken line*) measured at 77 K of (a) Pt-Br-Pt-II and (b) Pt-Br-Pd. Both the excitation lights (E_{ex}) and the transmission lights (E) are polarized parallel to the b axis. Insets show PESR spectra (derivative of absorption) at 4 K for the excitation of 3.1 eV. (Reprinted figure from [52])



inverted triangles for band \mathbf{a}_1 in Pt-Br-Pd. The thin solid line is the absorption spectra (ε_2) due to the CT excitons obtained from the polarized reflectivity spectra and their peaks correspond to E_{CT} . As seen, in Pt-Br-Pt-II, CT excitons do not contribute to the generation of band γ , but contribute to band α . Band γ in Pt-Br-Pt-II and band \mathbf{a}_1 in Pt-Br-Pd were generated only for the excitation energies higher than E_{CT} .

PESR measurements were also performed to investigate whether the photoproducts have spins ($S = 1/2$) or not. In Pt-Br-Pt-II, an ESR signal was observed in an as-grown single crystal. The ESR signal was enhanced by the photoirradiations. The inset in Fig. 2.9a showed the increased component (the PESR signal) for the 3.1 eV excitation. The excitation profile of the integrated intensities of PESR signals was shown by solid squares in Fig. 2.10a. Paramagnetic spins were produced by the 2.5-eV excitation. The same excitation did not generate band γ but enhances bands α and β so that the PESR signals in Pt-Br-Pt-II should be related to bands α and β . In those measurements, it could not be determined whether band γ is related to a spin ($S = 1/2$) or not.

In Pt-Br-Pd, on the other hand, no ESR signal was detected in an as-grown single crystal. The PESR signal by the 3.1 eV excitation was shown in the inset of Fig. 2.9b and the excitation profile of the integrated intensities of PESR signals was

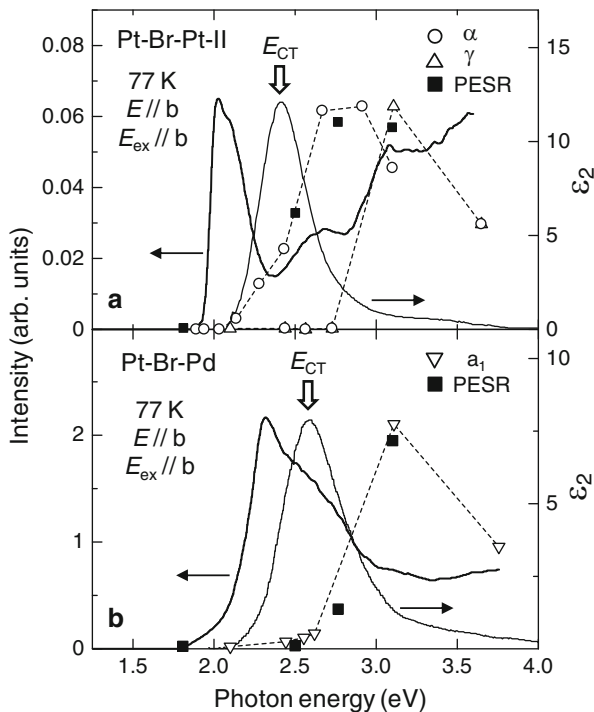


Fig. 2.10 Excitation profiles for the intensities of the PA bands (*open marks*), the PESR (*solid squares*), and the luminescence (*thick solid lines*) at 77 K in (a) Pt-Br-Pt-II and (b) Pt-Br-Pd. *Thin solid lines* show the imaginary part of the dielectric constants ϵ_2 . (Reprinted figure from [52])

shown by solid squares in Fig. 2.10b. The PESR signals were observed only by the excitations above 2.7 eV. Such a behavior is in agreement with the excitation profile of the PA band a_1 , so that a_1 is associated with a spin ($S = 1/2$).

Since these PA bands were observed in the gap region, it is natural to consider that they are attributable to spin-solitons (S^0), charged-solitons (S^+ , S^-), or polarons (P^+ , P^-) [10, 16, 21]. Figure 2.11 shows the localized energy levels of spin-solitons (S^0), charged-solitons (S^- and S^+), and polarons (P^- and P^+) in the case that the transfer energy t between the neighboring metal ions is equal to zero [21]. From this simplified picture, we can understand that S^0 , P^+ , and P^- have spin $S = 1/2$, and S^+ and S^- have no spin, while S^+ , S^- , P^+ , and P^- have a charge. The more realistic electronic structures of these gap states with a finite t are presented schematically in Fig. 2.12. Several groups reported theoretical absorption spectra of the gap states obtained based upon the 1D extended Peierls-Hubbard model [27, 33–35, 47]. Their spectral features are essentially the same; two absorption bands arise for a polaron, and one midgap band arises for either a spin- or charged-soliton.

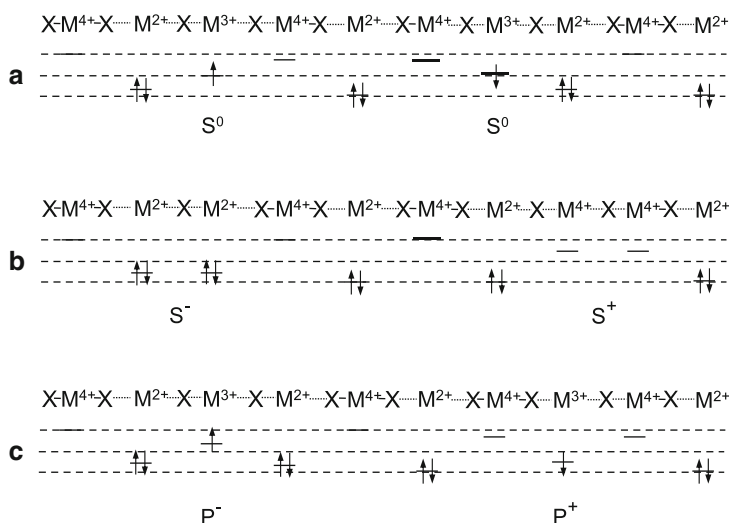


Fig. 2.11 Localized energy levels of (a) spin-solitons (S^0), (b) charged-solitons (S^- , S^+), and (c) polarons (P^- , P^+) (Reprinted figure with permission from [5])

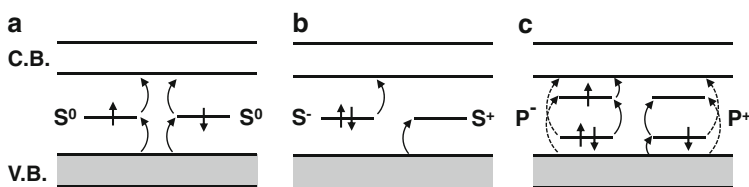


Fig. 2.12 Schematic electronic structures: (a) spin-solitons (S^0), (b) charged-solitons (S^- , S^+), and (c) polarons (P^- , P^+) (Reprinted figure with permission from [5])

In Fig. 2.12, the solid arrows indicate the possible optical transitions. For a polaron, it was theoretically revealed that oscillator strengths of the transitions indicated by broken arrows are extremely weak.

Taking into account the theoretical expectations shown in Fig. 2.12, a doublet structure a_1 and a_2 related to spins ($S = 1/2$) in Pt–Br–Pd could be assigned to polarons. It should be noted that in Pt–Br–Pd, electron polarons exist on the Pt sites and hole polarons on the Pd sites and therefore, the electron–hole asymmetry exists. In this case, PA energies for a positively charged polaron and a negatively charged one will be different from each other due to the difference in the magnitude of U on the metal sites. Thus the large spectral width of band a_2 was attributed to the superposition of the two transitions slightly split due to the electron–hole asymmetry.

In Pt–Br–Pt-II, bands α , β and band γ have different origins as mentioned above. The important information is that PA bands α and β were not detected in Pt–Br–Pd. Pt–Br–Pd has the nondegenerate CDW state, so that solitons should not be stabilized. These results suggested that bands α and β could be attributed to

solitons. Considering that bands α and β are associated with spins, solitons responsible for α and β should be spin-solitons. A simple model shown in Fig. 2.12 expects that a single midgap absorption arises for a spin-soliton. However, the observed PA consists of a doublet structure α and β and is located at the higher energy than $E_{CT}/2$. These experimental features could be explained by the theoretical studies; Iwano et al. showed that the absorption band of a spin-soliton is split under the presence of quantum lattice fluctuations [33] and its energy is higher than $E_{CT}/2$ due to the effect of on-site Coulomb repulsion U [51]. Thus, PA bands α and β were reasonably assigned to spin-solitons.

The energy of band γ is small, being about $0.3 \times E_{CT}$, so that band γ was assigned to the lower energy transition of polarons, which correspond to a_2 band in Pt–Br–Pd. In fact, the lower energy transitions of polarons are observed at around $0.37 \times E_{CT}$ in Pr–Br–Pd. In another Pt–Br chain compound, $[Pt(chxn)_2][Pt(chxn)_2Br_2]Br_4$ ($chxn$ = cyclohexanediamine), the similar low energy PA band was also observed at $0.35 \times E_{CT}$ (not shown) [37]. Moreover, the excitation profile of polarons (band a_1) in Pt–Br–Pd is similar to that of band γ , as shown in Fig. 2.10. This also supports the assignment of band γ to the lower energy transition of polarons. The higher energy transition of polarons could not be identified in these studies. It was considered to be obscured by the strong PA band β .

2.3.3 Conversion of an Exciton to a Spin-Soliton Pair

In this section, we discuss the relaxation dynamics of photoexcited states in MX-chain compounds associated with excitons, solitons, and polarons. As mentioned above, two relaxation processes are considered to exist; radiative decay (PL) from STE and nonradiative decay via conversions to soliton or polaron pairs and their recombination. In order to clarify the interrelation of these two processes, excitation profiles of PL were measured and compared to those of PA signals in Pt–Br–Pt-II and Pt–Br–Pd, which were shown in Fig. 2.10 [5, 52].

The excitation profiles of PL from STE were shown by thick solid lines in Fig. 2.10. In Pt–Br–Pt-II, the intensity of PL begins to increase from the absorption edge at about 1.9 eV and then decreases sharply at around E_{CT} . Such a sharp decrease of PL corresponds to the increase of the generation efficiency of spin-soliton pairs. This suggests that a conversion from an exciton to a spin-soliton pair occurs. This interpretation was supported by the fact that in Pt–Br–Pd the PL intensity did not decrease for the excitations with the energy of E_{CT} and that the relative PL intensity in Pt–Br–Pd is more than one order of magnitude larger than that in Pt–Br–Pt-II (see Figs. 2.8 and 2.10).

Dynamical aspects of the exciton to spin-soliton conversion were also investigated by the time-resolved PL measurements. In Fig. 2.13, the time-integrated PL spectra due to STEs at 10 K were shown by solid lines, and time characteristics of PL were shown in the insets. PL dynamics were reproduced by a single exponential decay, as shown by the broken lines. The decay time τ is ~ 220 ps in Pt–Br–Pt-II and ~ 390 ps in Pt–Br–Pd. Those values are at least one order of

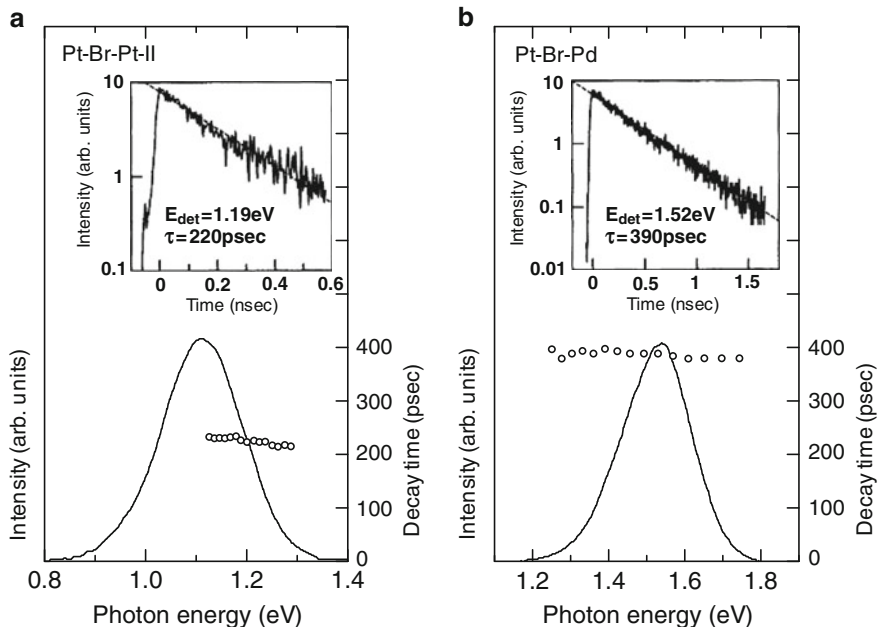


Fig. 2.13 Photoluminescence spectra (solid lines) and photoluminescence decay time τ (circles) at 10 K for the excitation energy of 3.2 eV in (a) Pt-Br-Pt-II and (b) Pt-Br-Pd. Both the excitation lights (E_{ex}) and the emission lights (E) are polarized parallel to the b axis. Insets show the time characteristics of photoluminescence for the detection energies of 1.19 eV in Pt-Br-Pt-II and 1.52 eV in Pt-Br-Pd. Broken lines show single exponential decays. (Reprinted figure from [52])

magnitude smaller than the radiative life time τ_r of STEs (4–6 ns) [20, 48], which was estimated from the oscillator strength of the CT-exciton transition in typical Pt compounds. This indicated that annihilations of STEs were dominated by nonradiative processes.

Figure 2.14 showed the temperature dependence of the decay time τ of PL in Pt-Br-Pt-II and Pt-Br-Pd, which was well reproduced by using the following formula as shown by the broken lines in Fig. 2.14.

$$\tau = [\tau_0^{-1} + \tau_a^{-1} \exp(-\Delta/kT)]^{-1} \quad (2.1)$$

The used parameter values were $\tau_0 = 225$ ps, $\tau_a = 115$ ps, and $\Delta = 9.5$ meV in Pt-Br-Pt-II, and $\tau_0 = 385$ ps, $\tau_a = 38$ ps, and $\Delta = 34$ meV in Pt-Br-Pd. The smaller values of τ (or Δ and τ_0) in Pt-Br-Pt-II compared to Pt-Br-Pd was considered due to the conversion from STEs to soliton pairs.

The theoretical studies based upon the 1D extended Peierls-Hubbard model provided detailed potential energy surfaces of the excited states for homometal CDW compounds, which were detailed in [22, 23, 51] and also in Chap. 8. The inset of Fig. 2.14 showed the cross section of the first and the second lowest potential surfaces as a function of intersoliton distance l_0 . The higher potential surface

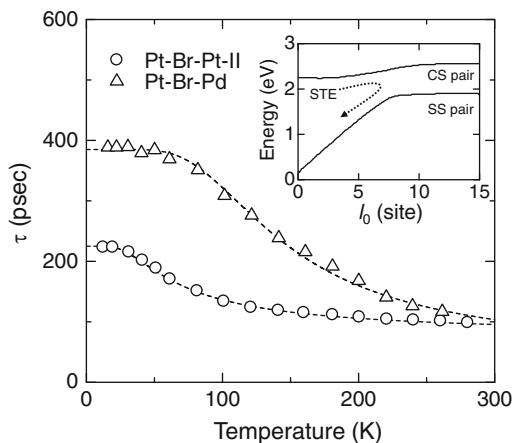


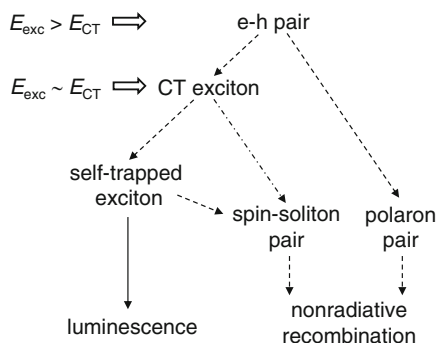
Fig. 2.14 Temperature dependence of the luminescence decay time τ . The detection energies are 1.19 eV in Pt-Br-Pt-II and 1.52 eV in Pt-Br-Pd. The inset shows the cross-section of the calculated potential energy surfaces (taken from [51]). SS and CS show a spin-soliton pair and a charged-soliton pair, respectively. (Reprinted figure from [52])

includes the STE and the charged-soliton pair and the lower surface includes the spin-soliton pair and is connected to the CDW ground state. With the parameters appropriate for MX-chain compounds, a spin-soliton pair is always the lowest energy excitation, although the energy difference between a spin-soliton pair and an STE is not so large [51].

According to more detailed theoretical analyses, a conversion from the STE to the spin-soliton pair was possible. These expectations were in good agreement with the experimental results of Pt-Br-Pt-II discussed above. In Pt-Br-Pt-II, it is reasonable to consider that Δ is a potential barrier between the STE and the spin-soliton pair and τ_0^{-1} is a tunneling rate through the barrier. We can imagine in the inset of Fig. 2.14 that such a barrier exists when the conversion from the STE to the spin-soliton pair occurs at large values of l_0 , e.g., larger than 8. In Pt-Br-Pd, the energy of potential surfaces is expected to increase sharply with increasing l_0 compared with that in Pt-Br-Pt-II (the inset of Fig. 2.14), so that the spin-soliton pair cannot be dissociated. This situation is analogous to bipolarons in nondegenerate conjugated polymers. In this case, the depth of the potential well around the STE should be increased. As a result, Δ was enhanced and τ_0^{-1} was decreased in Pt-Br-Pd relative to those values in Pt-Br-Pt-II. Thus, it is expected that the main relaxation path of STEs in Pt-Br-Pd is also the nonradiative recombination process through the solitonic states, which is essentially the same as that indicated by the arrows in the inset of Fig. 2.14 except for the slope of potential surfaces.

It is important to comment on the comparison of solitons in MX-chain compounds with those in *trans*-(CH)_x, in which nature of spin-solitons had also been extensively studied. In *trans*-(CH)_x, however, a conversion of an electron-hole

Fig. 2.15 Schematic diagram of the relaxation process of the photoexcited state in Pt–Br–Pt-II (Reprinted figure with permission from [5])



pair (the singlet B_u state) to a spin-soliton pair is essentially forbidden within the noninteracting electron model, due to the charge configuration symmetry in the bond ordered wave (BOW) ground state [64, 65]. Additional interactions (i.e., a second nearest-neighbor hopping [64]) which break the charge configuration symmetry, permit the conversion of the electron-hole pair to a spin-soliton pair. On the other hand, the MX-chain compounds are not charge configuration symmetric from the nature of CDW, so that photogeneration of spin-solitons is possible to occur. Moreover, in contrast to *trans*-(CH)_x, the excitonic effect is important in MX-chain compounds. Thus, the generation process of spin-solitons from the photoexcited states in MX-chain compounds is considerably different from that in *trans*-(CH)_x.

2.3.4 Overall Dynamics of Photoexcited States

The relaxation process of photoexcited states in Pt–Br–Pt-II was summarized in Fig. 2.15. Polarons are not generated from the CT exciton, since the energy of a polaron pair is much higher than the CT exciton. Polarons can be generated only from the higher energy excited states corresponding probably to the electron-hole continuum. CT excitons are relaxed to STEs. A part of STEs decay by PL, and the other parts are relaxed to spin-soliton pairs and then decay nonradiatively. CT excitons with large excess energies dissociate into spin-soliton pairs before stabilizing as STEs, since the generation efficiency of spin-solitons increases with increase of the excitation photon energy at around E_{CT} as seen in Fig. 2.10. This process is also shown by the dashed–dotted line in Fig. 2.15.

As mentioned in Sect. 2.2.2, Pt and Pd compounds having halogen ions as the counter anions show the 2D-ordered CDW states. In a typical example of such compounds, $[\text{Pt}(\text{chxn})_2][\text{Pt}(\text{chxn})_2\text{Br}_2]\text{Br}_4$, it was also demonstrated that photogenerations of solitons were suppressed [37] and only the photogeneration of polarons was observed. In general, in the compounds having 2D-ordered CDW states, PL intensities were relatively larger than that in the 1D CDW compounds as seen in Fig. 2.8, consistent with the result of the hetero-metal compound, Pt–Br–Pd.

When the bridging halogen displacement δ and the optical gap energy E_{CT} decrease and a compound approaches to the CDW-MH phase boundary, photoresponses are largely changed from those discussed here. A photoexcited state in the CDW ground state, that is, a M^{3+} pair is converted to a M^{3+} domain over several tens M^{3+} sites [66, 67]. In this case, the lowest photoexcited state of a M^{3+} pair cannot be regarded as an excitonic state, but the photoresponses should be regarded as a photoinduced phase transition from CDW to MH state. Such photoinduced CDW to MH transitions were indeed observed in $[Pd(chxn)_2][Pd(chxn)_2Br_2]Br_4$ and $[Pt(chxn)_2][Pt(chxn)_2I_2]I_4$ [66, 67]. In the latter compound, the photoinduced CDW to metal transition was also found in the case of strong photoexcitations. Photoinduced phase transitions in those MX-chain compounds are discussed in Chap. 5 in detail.

2.4 Summary

In this chapter, we reviewed the tunability of the CDW states in MX-chain compounds. By substituting the metals ($M = Pt, Pd, \text{ and } Ni$), the bridging halogens ($X = Cl, Br, \text{ and } I$), and the ligand molecules and the counter anions surrounding MX chains, the amplitude of CDW, the degeneracy of CDW, and the optical gap energy could be widely controlled. On the basis of such controls of the CDW states, nature of photoexcited states, i.e., excitons, solitons, and polarons, was investigated. From the comparative studies of the degenerate and nondegenerate CDW compounds using photoluminescence, photoinduced absorption, and photoinduced electron spin resonance measurements, the photoinduced gap states were clearly characterized as spin-solitons and polarons. By comparing the excitation profiles of the photoinduced absorption signals due to spin-solitons and the photoluminescence from self-trapped excitons, it was demonstrated that the luminescence process competes with the dissociation to spin-soliton pairs and the subsequent nonradiative decay. The detailed analyses of the temperature dependence of the photoluminescence decay time revealed that a conversion from a self-trapped exciton to a spin-soliton pair occurs through a finite potential barrier, the magnitude of which depends on the degeneracy of CDW. Such an exciton to a spin-soliton pair conversion could be explained by the theoretical simulations based upon the 1D-extended Peierls–Hubbard model. Thus, a spin-soliton pair is the lowest energy excitation, so that it plays dominant roles on the relaxation process of photoexcited states in MX-chain compounds having CDW ground states.

On the basis of these fundamental studies on the CDW states, a great deal of efforts for designs and syntheses of new MX-chain compounds and explorations of new phenomena have been made. As a result, a variety of novel physical properties such as gigantic nonlinear optical responses and ultrafast-photoinduced phase transitions have been discovered. The details of them are reviewed in the following several chapters from both experimental and theoretical points of view.

References

1. Whitfield G, Shaw PB (1976) *Phys Rev B* 14:3346
2. For a review, see Heeger AJ, Kivelson S, Schrieffer JR (1988) *Rev Mod Phys* 60: 781
3. Su WP, Schrieffer JR, Heeger AJ (1979) *Phys Rev Lett* 42:1698
4. Su WP, Schrieffer JR, Heeger AJ (1980) *Phys Rev B* 22:2099
5. Okamoto H, Yamashita M (1998) *Bull Chem Soc Jpn* 71:2023
6. Tanino H, Kobayashi K (1983) *J Phys Soc Jpn* 52:1446
7. Nasu K (1984) *J Phys Soc Jpn* 52:3865
8. Nasu K (1984) *J Phys Soc Jpn* 53:302
9. Nasu K (1984) *J Phys Soc Jpn* 53:427
10. Ichinose S (1984) *Solid State Commun* 50:137
11. Tanaka M, Kurita S, Okada Y, Kojima T, Yamada Y (1985) *Chem Phys* 96:343
12. Tanino H, Koshizuka N, Kobayashi K, Yamashita M, Hoh K (1985) *J Phys Soc Jpn* 54:483
13. Wada Y, Mitani T, Yamashita M, Koda T (1985) *J Phys Soc Jpn* 54:3143
14. Matsushita N, Kojima N, Ban T, Tsujikawa I (1987) *J Phys Soc Jpn* 56:3808
15. Kuroda N, Sakai M, Nishina Y, Tanaka M, Kurita S (1987) *Phys Rev Lett* 58:2212
16. Onodera Y (1987) *J Phys Soc Jpn* 56:250
17. Kurita S, Haruki M, Miyagawa K (1988) *J Phys Soc Jpn* 57:1789
18. Haruki M, Kurita S (1988) *Phys Rev B* 39:5706
19. Wada Y, Era K, Yamashita M (1988) *Solid State Commun* 67:953
20. Tanino H, Rühle W, Takahashi K (1988) *Phys Rev B* 38:12716
21. Baeriswyl D, Bishop AR (1988) *J Phys C* 21:339
22. Mishima A, Nasu K (1989) *Phys Rev B* 39:5758
23. Mishima A, Nasu K (1989) *Phys Rev B* 39:5763
24. Matsushita N, Kojima N, Watanabe N, Tsujikawa I (1989) *Solid State Commun* 71:253
25. Donohoe RJ, Ekberg SA, Tait CD, Swanson BI (1989) *Solid State Commun* 71:49
26. Wada Y, Mitani T, Toriumi K, Yamashita M (1989) *J Phys Soc Jpn* 58:3013
27. Tagawa Y, Suzuki N (1990) *J Phys Soc Jpn* 59:4074
28. Okamoto H, Toriumi K, Mitani T, Yamashita M (1990) *Phys Rev B* 42:10381
29. Wada Y, Yamashita M (1990) *Phys Rev B* 42:7398
30. Kuroda N, Sakai M, Suezawa M, Nishina Y, Sumino K (1990) *J Phys Soc Jpn* 59:3049
31. Okamoto H, Okaniwa K, Mitani T, Toriumi K, Yamashita M (1991) *Solid State Commun* 77:465
32. Okamoto H, Mitani T, Toriumi K, Yamashita M (1992) *Mater Sci Eng B* 13:L9
33. Iwano K, Nasu K (1992) *J Phys Soc Jpn* 61:1380
34. Gammel JT, Saxena A, Batistic I, Bishop AR, Phillips SR (1992) *Phys Rev B* 45:6408
35. Webber-Milbrodt SM, Gammel JT, Bishop AR, Lor EY Jr (1992) *Phys Rev B* 45:6435
36. Donohoe RJ, Worl LA, Arrington CA, Bulou A, Swanson BI (1992) *Phys Rev B* 45:13185
37. Okamoto H, Mitani T, Toriumi K, Yamashita M (1992) *Phys Rev Lett* 69:2248
38. Sakai M, Kuroda N, Suezawa M, Nishina Y, Sumino K, Yamashita M (1992) *J Phys Soc Jpn* 61:1326
39. Okamoto H, Toriumi K, Mitani T, Yamashita M (1992) *Mol Cryst Liq Cryst* 218:247
40. Okamoto H, Mitani T (1993) *Prog Theor Phys Suppl* 113:191
41. Okamoto H, Mitani T, Toriumi K, Yamashita M (1993) *Synth Met* 55:524
42. Kuroda N, Ito M, Nishina Y, Kawamori A, Kodera Y, Matsukawa T (1993) *Phys Rev B* 48:4245
43. Kuroda N, Ito M, Nishina Y, Yamashita M (1993) *J Phys Soc Jpn* 62:2237
44. Ooi H, Yamashita M, Kobayashi T (1993) *Solid State Commun* 86:789
45. Ooi H, Yoshizawa M, Yamashita M, Kobayashi T (1993) *Chem Phys Lett* 210:237
46. Tagawa Y, Suzuki N (1995) *J Phys Soc Jpn* 64:1800
47. Tagawa Y, Suzuki N (1995) *J Phys Soc Jpn* 64:2212
48. Wada Y, Lemmer U, Gobel EO, Yamashita M, Toriumi K (1995) *Phys Rev B* 52:8276

49. Okamoto H, Oka Y, Mitani T, Yamashita M (1997) *Phys Rev B* 55:6330
50. Okamoto H (1997) In: Nasu K (ed) *Relaxations of excited states and photoinduced structural phase transitions*. Springer, Berlin, p 92
51. Iwano K (1997) *J Phys Soc Jpn* 66:1088
52. Okamoto H, Kaga Y, Shimada Y, Oka Y, Iwasa Y, Mitani T, Yamashita M (1998) *Phys Rev Lett* 80:861
53. Toriumi K, Wada Y, Mitani T, Bandow S, Yamashita M, Fujii Y (1989) *J Am Chem Soc* 111:2341
54. Toriumi K, Okamoto H, Mitani T, Bandow S, Yamashita M, Wada Y, Fujii Y, Clark RJH, Michael DJ, Edward AJ, Watkin D, Kurmoo M, Day P (1990) *Mol Cryst Liq Cryst* 181:333
55. Okamoto H, Shimada Y, Oka Y, Chainani A, Mitani T, Toriumi K, Inoue K, Manabe T, Yamashita M (1996) *Phys Rev B* 54:8438
56. Okaniwa K, Okamoto H, Mitani T, Toriumi K, Yamashita M (1991) *J Phys Soc Jpn* 60:997
57. Pauling L (1960) *The nature of the chemical bond*, 3rd edn. Cornell University Press, New York
58. Muller O, Roy R (1974) *The major ternary structural families*. Springer, New York
59. Lide DR, Lide Jr (1998) *Handbook of chemistry and physics*, 79th edn. CRC press, Boca Raton, FL
60. Tomimoto S, Nansei H, Saito S, Suemoto T, Sakata K, Takeda J, Kurita S (1998) *Phys Rev Lett* 81:417
61. Tomimoto S, Saito S, Suemoto T, Sakata K, Takeda J, Kurita S (1999) *Phys Rev B* 60:7961
62. Matsuoka T, Suemoto T, Takeda J, Kurita S (2003) *Phys Rev Lett* 91:247402
63. Dexheimer SL, Van Pelt AD, Brozik JA, Swanson BI (2000) *Phys Rev Lett* 84:4425
64. Kivelson S, Wu W-K (1986) *Phys Rev B* 34:5423
65. Takimoto J, Sasai M (1989) *Phys Rev B* 39:8511
66. Matsuzaki H, Yamashita M, Okamoto H (2006) *J Phys Soc Jpn* 75:123701
67. Kimura K, Matsuzaki H, Takaishi S, Yamashita M, Okamoto H (2009) *Phys Rev B* 79:075116

Material Designs and New Physical Properties in MX-
and MMX-Chain Compounds

Yamashita, M.; Okamoto, H. (Eds.)

2013, X, 270 p., Hardcover

ISBN: 978-3-7091-1316-5